MC decomposition and boride formation in a next generation polycrystalline Ni based superalloy during isothermal exposure at 900 °C

Kitaguchi, H.S.; Small, L.; Jones, I.P.; Chiu, Y.L.; Hardy, M.C.; Bowen, P.

DOI:
10.1016/j.matchar.2024.113721

Document Version
Publisher's PDF, also known as Version of record

Citation for published version (Harvard):
Kitaguchi, HS, Small, L, Jones, IP, Chiu, YL, Hardy, MC & Bowen, P 2024, 'MC decomposition and boride formation in a next generation polycrystalline Ni based superalloy during isothermal exposure at 900 °C', *Materials Characterization*, vol. 209, 113721. https://doi.org/10.1016/j.matchar.2024.113721

Materials Characterization 209 (2024) 113721

Contents lists available at ScienceDirect

Materials Characterization

journal homepage: www.elsevier.com/locate/matchar

MC decomposition and boride formation in a next generation polycrystalline Ni based superalloy during isothermal exposure at 900 °C

H.S. Kitaguchi [a,*], L. Small [a], I.P. Jones [a], Y.L. Chiu [a], M.C. Hardy [b], P. Bowen [a]

[a] School of Metallurgy and Materials, College of Engineering and Physical Science, The University of Birmingham, Edgbaston, Birmingham B15 2TT, UK
[b] Rolls-Royce plc, PO Box 31, Derby DE24 8BJ, UK

ARTICLE INFO

Keywords:
Superalloys
Iso-thermal treatment
Carbides: MC $M_{23}C_6$
Borides: M_5B_3 M_3B_2
TEM
EDS
Thermo-Calc software

ABSTRACT

Detailed microstructural characterisation of phases present in a next generation polycrystalline Ni based superalloy after thermal exposure at 900 °C was carried out, focusing on carbides and borides. Metastable M_5B_3 precipitated after 32 h had a stoichiometry of $(Cr_{0.7}Mo_{0.2}W_{0.1})_5B_3$ with substitutions with Ni, Co, Nb and Ta. Fine $M_{23}C_6$ (a = 10.62 Å) was overgrown by metastable M_5B_3, as shown by rigorous TEM-SAD pattern investigation. The borides were eventually dominated by Mo rich M_3B_2, at the apparent expense of MC. Decomposition of MC was confirmed; it transformed sequentially to γ and then γ′. The primary driving force for the MC decomposition was attributed to γ′ precipitation, increasing its fraction to the thermodynamic equilibrium at 900 °C.

1. Introduction

Polycrystalline nickel-based superalloys, used for turbine discs, operate at high temperatures and high tensional pressures and must satisfy various physical and mechanical requirements, from oxidation/corrosion resistance to monotonic tensile strength, creep and low cycle fatigue resistance and damage tolerance [1,2]. Superior mechanical properties are conferred by Ni_3Al based γ′ hardening precipitates, which have an $L1_2$ ordered structure, perfectly coherent with the disordered γ face-centred cubic (fcc) matrix, which is composed mainly of Ni, Co and Cr [1]. Thanks to multiple refractory metal alloying elements such as Ti, Mo and W, as well as interstitial elements carbon and boron, other phases than γ and γ′ can precipitate and, in particular, carbides and borides have been found to play a significant role, although the exact role of those precipitates has proven controversial [2].

Primary carbides in Ni superalloys are often denoted MC where M stands for a metal atom, mainly Ti, Ta and/or Nb [1] dependent on the alloy composition, with a stoichiometric ratio of 1:1 for the metal to carbon ratio. They could form in the liquid phase [2,3]. Other carbides, such as M_6C, M_7C_3 and $M_{23}C_6$, can also form during ageing and protracted periods of service exposure, often accompanied by the decomposition of MC due to its thermodynamic instability at intermediate temperatures up to 1100 °C, decomposing to carbides with a smaller stoichiometric fraction of carbon [4]. Those reactions are often expressed as $MC + \gamma \rightarrow M_{23}C_6 + \gamma'$ [3] with Cr usually dominant in the $M_{23}C_6$ [1] and $MC + \gamma \rightarrow M_6C + \gamma'$ [5] with Mo and W rich in the M_6C [1]. Undesirable intermetallics can form by the reaction $MC + \gamma \rightarrow M_{23}C_6/M_6C + \sigma + \eta$ [6–9], where σ and η are described as (Mo, W)-rich with Ni and Co partitioning [10] and Ni_3(Ti, Ta)-based [6], respectively, depending on the alloy composition and on the temperature.

Boron was originally introduced as a grain boundary (GB) strengthening element, improving the creep-rupture resistance [1]. There is, however, an ongoing debate concerning the general effect of boron on polycrystalline Ni based alloys. Improved ductility and creep rupture life on increasing boron concentration [11] and the confirmation of boron segregating to GBs [12,13] suggested an improved GB cohesion [14]. Recent research has attempted to rationalise the mechanical properties, including via post-mortem analyses of stress rupture tests [15], in-situ strain field analyses [16] and high resolution microstructural observations aimed at understanding both chemical segregation and precipitation at phase boundaries [15–19]. They discussed the role of borides [19], including interactions of these precipitates with GBs, particularly at serrations in the GBs [12,16].

There are in general three commonly observed borides in Ni superalloys: M_5B_3, M_3B_2, M_2B depending on metal-boron stoichiometry. In general, they have the same structure: a tetragonal with a similar lattice parameter to the a axis lattice spacing of 5-6 Å. Thanks to high resolution TEM, atomic column imaging and more detailed microstructural studies suggested rather complex structures [20,21]. M_2B can exhibit multiple variants within the precipitate, separated by stacking faults containing

* Corresponding author.
E-mail address: h.kitaguchi@bham.ac.uk (H.S. Kitaguchi).

https://doi.org/10.1016/j.matchar.2024.113721
Received 6 November 2023; Received in revised form 25 January 2024; Accepted 30 January 2024
Available online 1 February 2024

an orthorhombic structure [20]. During studies of high boron content alloys with coarsened M_3B_2 and M_5B_3, they were found coexisting within a particle, exhibiting a perfect matching of a tetragonal-tetragonal alignment [21]. The chemistry of the borides was studied by Gupta et al. [19]; fine M_5B_3 showed chemical inhomogeneities within a precipitate, interpreted as potential phase transformations [19].

A newly developed polycrystalline Ni superalloy: New Alloy has been studied here. Considering development in various future applications and components, its microstructural evolution after thermal exposure at 900 °C was studied, mainly based on electron microscopy and focusing on carbides and borides.

2. Methodology

2.1. Material

The Ni superalloy: New Alloy was prepared via a powder-route. It was polycrystalline with a chemical composition as specified in Table 1. It was thermo-mechanically treated at a temperature above the γ′ solvus before being cooled rapidly to room temperature at a rate close to 100 °C/s to homogenise and to keep the microstructure as close as possible at the solution heat treatment temperature. The average grain size was 6 μm in diamter. Some specimens were heat treated isothermally at 900 °C for 1 h (sample ID HT_1), 32 h (HT_32), 160 h (HT_160) and 480 h (HT_480). The as-quenched sample was designated HT_0.

2.2. SEM imaging and analysis

SEM imaging was carried out using a JEOL JSM 7000-F SEM with an electron acceleration voltage of 20 keV and using a backscattered electron (BSE) detector. Each sample was mechanically polished with the final polish using a colloidal silica solution. For quantitative image analyses, each sample was imaged at a fixed magnification of x2,500. Four micrographs were acquired per location and five locations were arbitrarily chosen. This resulted in 20 micrographs per sample. Image-J Software (Image-J) was used to quantify the fractions of the phases present. To obtain a consistent outcome, the grey scale to be counted was set above 180 and binary micrographs were produced using the automated function in Image-J. The pixel size was 38 nm. Particles <80 nm in diameter, approximately 4 pixels, were discarded as noise.

2.3. SEM-EDS and image analysis

SEM-EDS mapping with an acceleration voltage of 10 keV was carried out using the same sample polishing method as described in Section 2.2, and an Oxford Instruments Ultim Max EDS detector and Aztec EDS Software: Ver. 6.0. Quantitative image analyses using the EDS maps were carried out to analyse the area fractions of the different phases present. After deconvolution of over-lapping characteristic x-rays, EDS maps for each element in the alloy were produced. Following the SEM image analysis, a fixed analysis method was applied to minimise uncertainty, involving a fixed grey scale value and an automatic binary conversion using Image-J, before measuring the area fraction of each element. Deviations of each image analysis with 2σ: 95% confidence were calculated and regarded as corresponding errors in the results.

2.4. XRD

Powder XRD analyses yielding γ and γ′ lattice parameters to support the TEM analyses were carried out using a metallographic samples of surface area of approx. 5x10mm. A Proto AXRD powder diffractometer operating at 30 kV/20 mA using Cu Kα radiation was used with a step size of 0.015° over a 2θ range between 70 and 100°, including the (220), (113) and (222) reflections for the γ and γ′ phases. For the lattice parameter determinations, peak fit analyses were carried out using OriginPro 2023b. Following estimations of the two peak summits per diffraction plane, automated peak fitting using a Gaussian distribution-based model was carried out to refine the γ and γ′ peak areas and their positions. Analyses from the three sets of planes yielded three inter-planar spacings, hereafter d-spacings, per phase, followed by calculations of an average value of the lattice constants.

2.5. TEM: Sample preparation, TEM and TEM-EDS

A Philips TECNAI F20 TEM and a JEM 2100 TEM, both operated at 200 keV, were used for TEM and STEM-EDS analyses, coupled with an Oxford Instruments X-MAX 40 detector with Aztec EDS Ver. 6.0. Camera lengths were calibrated using a standard Si thin film. For the general microstructural observations, samples were produced by machining and then polishing the material to a thickness of 0.5 mm and 0.2 mm, respectively. They were spark eroded into 3 mm diameter discs, which were subsequently subjected to twin-jet electro-polishing using a solution of 5% perchloric acid in methanol at −30 °C at a voltage of $20V_{dc}$. For site-specific sample preparation, a Thermo Fisher Quanta 3D FIB-SEM was used. Crystallographic analyses to determine a crystal structure as well as lattice parameters were carried out at least three different beam directions. At least two d-spacings of the two diffraction planes and the composing angle were measured. These were compared with the expected crystal structure and lattice parameter. The predicted and measured values differed by <2%. Experimental tilt angles were recorded using a Gatan TEM double tilt holder and practical TEM thin foil tilt angles were calculated, following Ref. [23]. They were compared with theoretical values in accordance with the determined crystal structure, lattice parameters and the beam directions, which are shown in the figures between pairs of diffraction patterns with the experimental and the theoretical values presented respectively as a number followed by one in brackets.

TEM-EDS k factor determinations were carried out for each alloying metal element following Ref. [24] with a ratio standard element of Cr Kα. Kα characteristic x-rays were generally used for the quantification, except for Ta M-series and W L-series. Counting statistical errors determined by Aztec were found to be <3 % for the major elements. Minor elements with concentration <2 at.% showed errors as large as 20 %.

2.6. Software aided simulations

Thermo-Calc Software, hereafter Thermo-Calc, with data base TTNI8 was used to predict phase fractions at given temperatures [25]. Manual iteration processes were carried out by excluding phases unidentified in experimental work in the temperatures of interest. TEM diffraction patterns based on the structures and chemistries were predicted by Crystal Maker Software SingleCrystal 4 [26]. Atomic distances/angles and visualisations of atom configurations within the unit cell were also predicted and displayed by the software.

Table 1
New Alloy chemical compositions in range in weight percent (wt%) [22].

Wt%	Ni	Al	Ti	Cr	Co	Mo	Nb	W	Zr	Ta	Fe	Mn	Si	C	B
Min	Bal	2.9	2.6	11.5	14.6	2.0	1.2	3.3	0.05	3.5	0.8	0.2	0.1	0.02	0.01
Max		3.3	3.1	13.0	15.9	2.4	1.8	3.7	0.11	5.1	1.2	0.6	0.6	0.06	0.03

3. Results

3.1. Qualitative characterisations using SEM (-EDS) and XRD

Fig. 1a to e show representative BSE SEM micrographs used for the area fraction analysis from HT_0: without thermal exposure through to HT_480: the longest exposure of 480 h. The number and size of the bright particles increased following thermal exposure. There is also an increasing tendency for the particles to inhabit grain boundaries. Area fraction analyses of the bright particles were carried out. The binary micrographs corresponding to Fig. 1a-e, used for the quantitative analysis, are shown in Fig. 1f-j. Fig. 2 shows a graph of the area fraction against the heat treatment duration. Each data point represents an image analysis. Considering the 20 micrographs, it was found that the area fraction of the bright particles increased parabolically from HT_0 to HT_480, from approximately 0.3% to 0.6%.

Fig. 3 shows EDS maps for HT_0. The particles were (Ta, Nb, Ti) carbides, presumably MC primary carbides [1]. Figs. 4–6 show maps for the heat treated samples. The particles become rich in Mo and W which enrichment always coincides each other. Mo and W are known to partition in borides, so this may indicate the precipitation of borides, which are later confirmed in the following sections. Taking advantage of similar cross-sections and absorption coefficients of Nb L characteristic x-ray (the MC constituent) and Mo L x-ray (the putative boride constituent), quantitative area fraction analyses were attempted, as shown in Fig. 7, after acquiring four individual EDS maps per heat treatment time. Mo enriched particles began to appear after 32 h (HT_32: Fig. 7b) and became predominant particles after HT_160: Fig. 7c. An average area ratio of Nb-L to Mo-L per annealing time was calculated. Combining the particle area fractions analysed via the SEM-BSE images with the EDS mapping image analyses resulted in Fig. 8a: quantitative area fractions of MC and borides up to 480 h. Phase balance predictions were conducted using Thermo-Calc with the chemical composition of measured values within the specification of Table 1; the presence of both MC and M_3B_2 at 900 °C was predicted, as shown in Fig. 8b (see the vertical dashed line).

Powder XRD measurements of γ and γ′ precipitates were carried out. (200), (131) and (222) reflections were chosen for analyses of γ and γ′. After peak deconvolution, the evolution of peak area ratios between γ and γ′ from HT_0 to HT_480 was measured, as well as the peak postions. γ′ was found to have a positive misfit with the γ matrix at room temperature; this is in line with other polycrystalline Ni based superalloys, such as RR1000 [27]. As shown in Table 2, the average lattice parameters between HT_0 and HT_480 vary from 3.585 and 3.890 to 3.594 and 3.602 Å for γ and γ′, respectively, with a typical error of 0.3% of the average values.

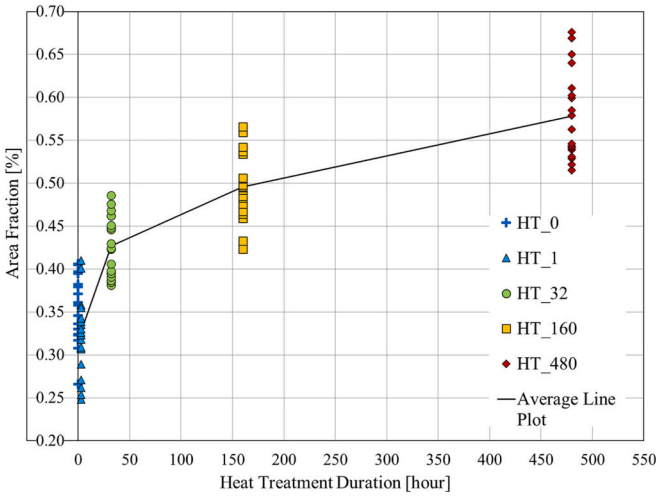

Fig. 2. Quantitative SEM particle image analysis results, plotting each analysed micrograph.

3.2. TEM (-EDS)

3.2.1. Site specific TEM sample: adjoining MC and boride using HT_32

Fig. 9a and b show an SEM micrograph of adjoining MC (Ti, Ta and Nb rich) and the putative boride (Mo and W rich), found in the EDS mapping and a TEM bright field (BF) micrograph after FIB cross-sectional sample preparation, respectively. Fig. 9c and d show a STEM-BF micrograph and the same STEM-BF micrograph superimposed with EDS maps for Ti: blue and Mo: purple, respectively. MC was found to be round with the size of 500 nm as indicated by the arrow in Fig. 9c. Regarding the Mo and W rich, as pointed by the triangle it appeared as a rod shaped. It was also found to be enriched with Cr, as shown in Fig. 9e, which shows a filled (black) spectrum compared to a superimposed spectrum from the γ/γ′ matrix drawn with a line.

Crystallographic analyses of the boride particle using three different beam directions are shown in Fig. 10a-c using convergent beam electron diffraction (CBED). It is concluded that the particle has a tetragonal structure: a = 6.06 c = 3.23 Å (c/a = 0.533), characteristic of M_3B_2, (prototype V_3B_2: a = 5.73 c = 3.02 Å (c/a = 0.527) [28]). The same species was also confirmed using another precipitate with selective aperture diffraction (SAD) patterns as shown in Fig. 11. It was also noted that the boride adjacent to the MC did not exhibit a clear coherency with MC but showed coherency with the adjacent γ matrix as suggested by Fig. 10d, taken at the same tilt as Fig. 10c. The M_3B_2 was coherent with the lower side of γ as seen in the dark field (DF) micrograph in Fig. 10e

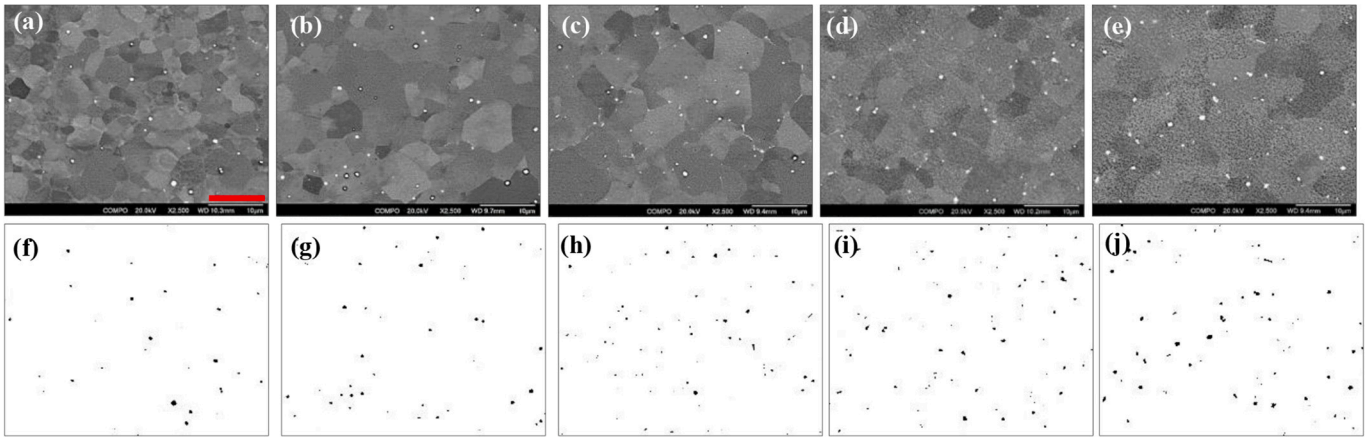

Fig. 1. (a)-(e) Representative micrographs for the particle image analysis for HT_0, HT_1, HT_32, HT_160, and HT_480, respectively. (f)-(j) Corresponding binary images for the quantitative analysis for HT_0, HT_1, HT_32, HT_160 and HT_480, respectively. The bar in bottom-left in (a) shows a 10 μm scale-bar.

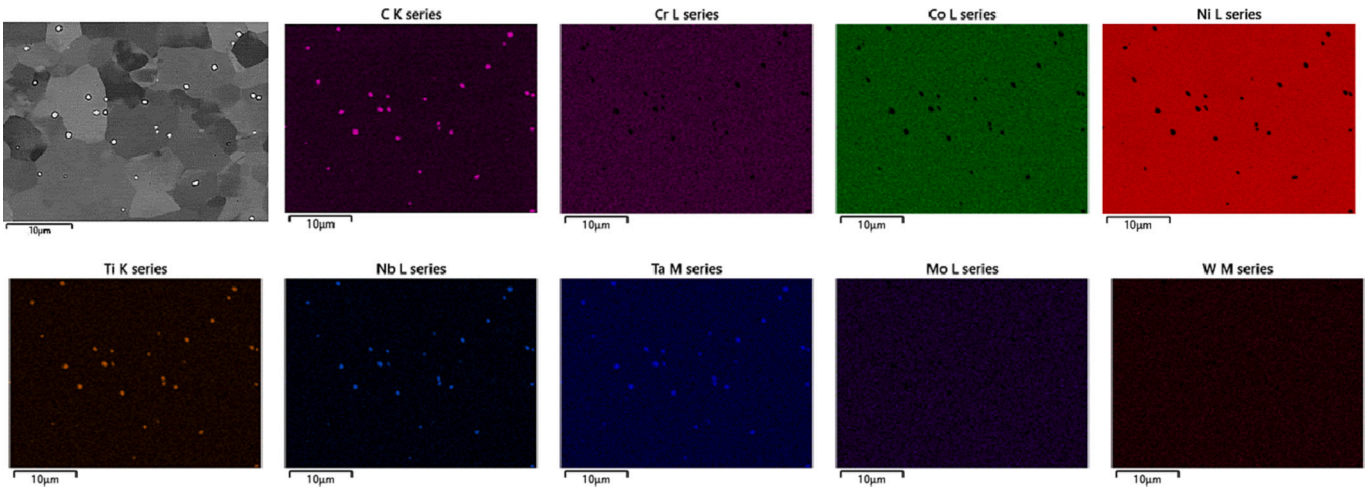

Fig. 3. Representative EDS mapping results of HT_0.

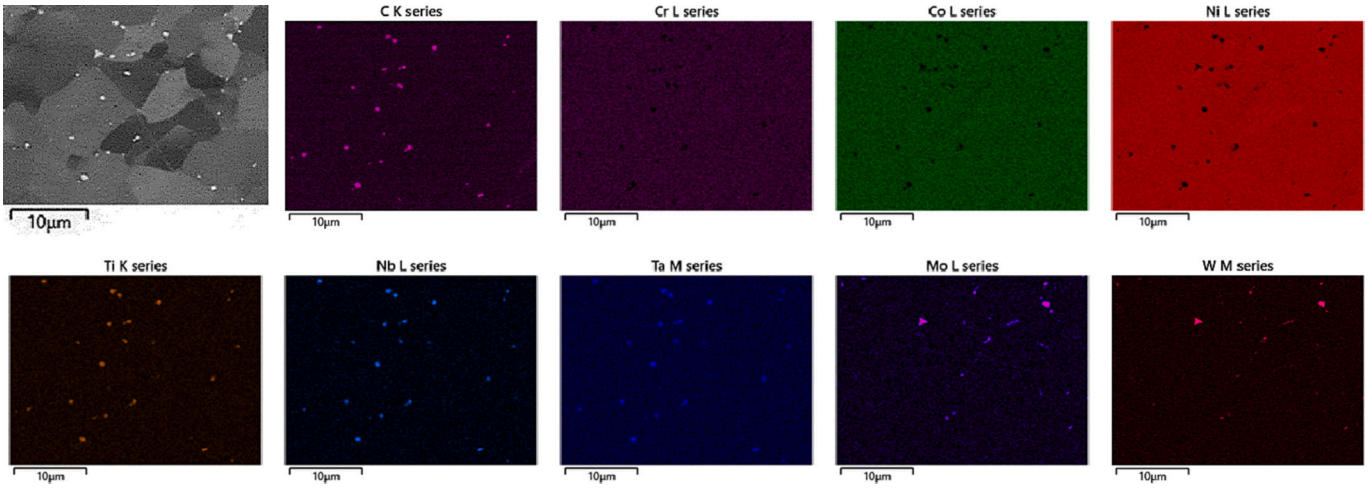

Fig. 4. Representative EDS mapping results of HT_32.

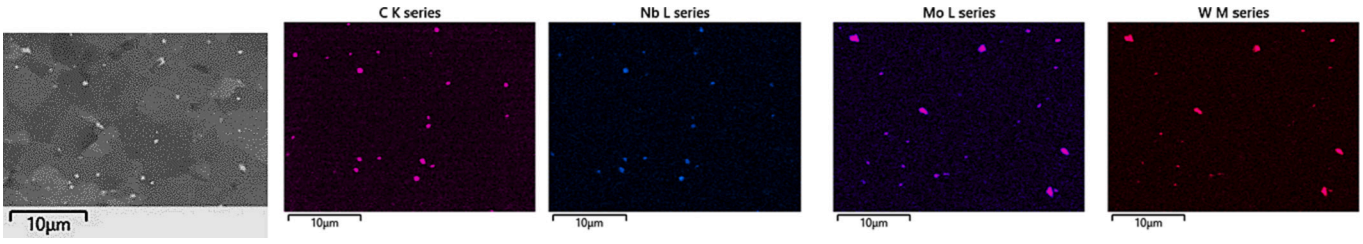

Fig. 5. Representative EDS mapping results of HT_160.

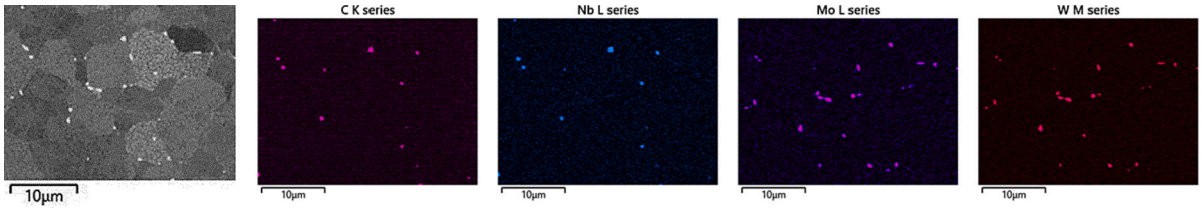

Fig. 6. Representative EDS mapping results of HT_480.

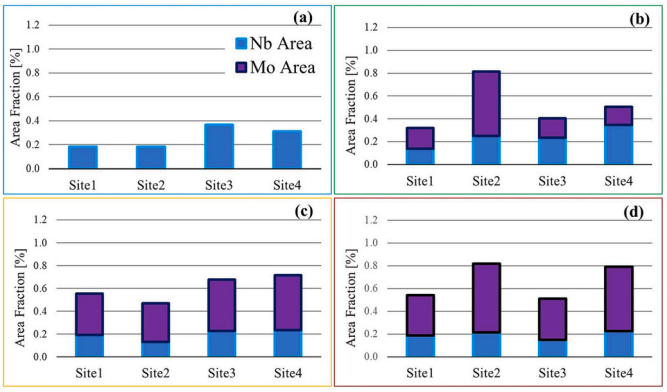

Fig. 7. Area fractions of Nb and Mo from four individual EDS mapping sites from four samples of HT_0, 32, 160 and 480 from (a) to (d), respectively.

using the matrix 002 diffraction. The crystallographic orientation relationship between the M_3B_2 and the matrix was $[\bar{1}20]_{M3B2} \| [\bar{1}10]_{\gamma}$ and $(2\bar{1}1)_{M3B2} \| (\bar{1}\bar{1}1)_{\gamma}$.

3.2.2. Thin foil TEM sample using HT_32 and HT_160

After exhaustive TEM thin foil observations, the major precipitates found in the current study were MC and intergranular M_3B_2 (Mo, W and Cr rich) as described in the previous section. Finer particles, sized 100–200 nm, were occasionally confirmed, as shown in Fig. 12 in HT_32. As shown in Fig. 12b, the Cr peak (5.4 keV) was higher than that in the M_3B_2 spectrum. Combining the identification of the boron Kα peak present in the EDS spectrum with the crystallographic analysis at different beam directions (Fig. 12c-f), the Cr rich fine particle was shown to be a tetragonal M_5B_3 type boride with a = 5.63 and c = 10.5 Å (c/a = 1.87) (prototype Cr_5B_3 (a = 5.446 c = 10.64 Å, c/a = 1.95)). Fig. 13 shows another example of an M_5B_3 precipitate, found in HT_32. As shown in Fig. 13a, the particle was present at a triple junction of high-angle grain boundaries (HAGBs). Each micrograph was taken at the same tilt, which corresponded exactly to a zone axis $B = [\bar{1}30]_{M5B3}$, as shown in Fig. 13d. It was found the borides are coherent with the bottom γ matrix grain for which $B = [00\bar{1}]_{\gamma}$, shown in Fig. 13a with a magnified micrograph in Fig. 13b. The SAD patterns showed an additional diffraction pattern shown in Fig. 13c (inset). A dark field (DF) micrograph, revealed a fine particle sized <100 nm embedded in the M_5B_3 particle at the triple junction.

Fig. 14a shows intensity profiles along (100) and $(\bar{1}00)$ for γ and γ′ with circular data points, superimposed with the M_5B_3 (Fig. 13d) and the fine particle profiles from Fig. 13c with square and triangular data points, respectively. The top-right line profile was generated by simulations and superimposed to the TEM-SAD experimental results. The simulated parameters were chosen as introduced below; γ/γ′ parameters in HT_32 were deduced from Table 2 as $a_{\gamma} = 3.586$ Å $a_{\gamma'} = 3.596$ Å. The M_5B_3 lattice parameters were used from the TEM-SAD analysis from Fig. 12. $M_{23}C_6$, often confirmed in austenitic steels and superalloys, was also included in the simulation with the lattice parameter taken from an ICDD database, measured with a pure Cr of $Cr_{23}C_6$: a = 10.66 Å [29]. Fig. 14b shows a magnified part of Fig. 14a focusing on the range 3.4–6.2 [1/Å*10], also with an extra x-axis labelled in real space at the top of Fig. 14b. Extraction of the experimental electron intensity and identifying the shape of the peak enable to study in a fine scale of peak positions. It is possible to identify that the $(200)_{\gamma/\gamma'}$ diffraction peak was at a smaller 1/d than $(310)_{M5B3}$ and the nearby diffraction peak from the fine precipitate shown in Fig. 13c. The simulation agreed with the TEM SAD patterns in that γ/γ′ have larger d values (smaller 1/d) than 310_{M5B3} or 600_{M23C6} which had extremely similar values to each other of 5.62 and 5.63 [1/Å*10], respectively. Thus from past literature and combining our experimental TEM and powder XRD, it is confidently concluded that the fine particle identified at the triple junction was an $M_{23}C_6$ particle with a lattice parameter of a = 10.62 Å. In addition, it is determined that there is coherency between the matrix and the boride;

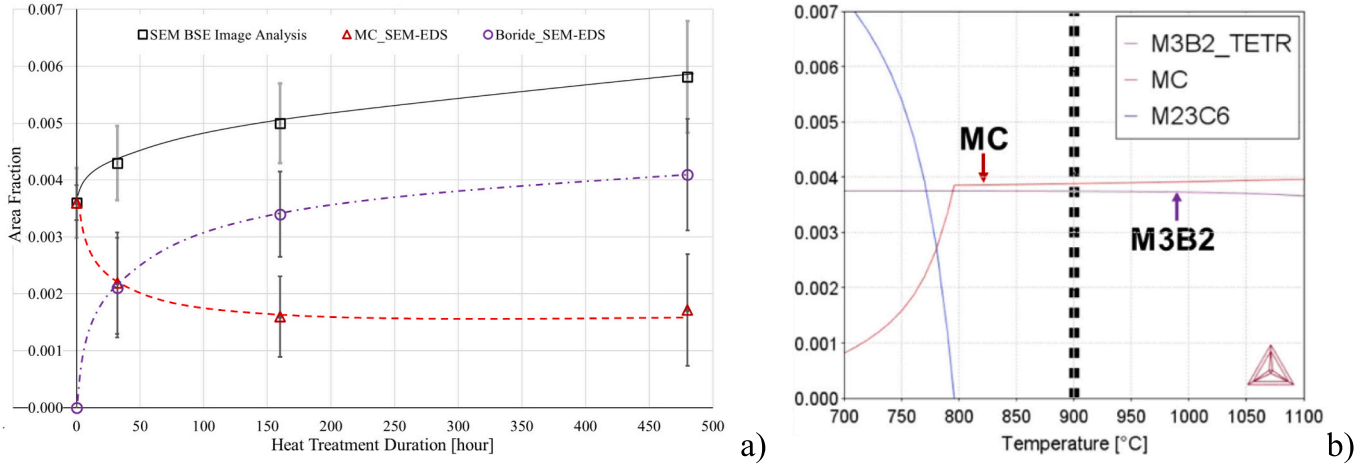

Fig. 8. (a) Area Fraction analyses of the MC and the predicted borides after combining the SEM-BSE and SEM-EDS measurements. (b) Thermo-Calc predictions; γ and γ′ were considered but not included in the figure.

Table 2
Summary of γ and γ′ lattice parameter analyses by XRD using (202) (131) and (222) planes.

Sample ID	γ [Å] (after analysing 202, 131 and 222 planes)			γ′ [Å] (after analysing 202, 131 and 222 planes)		
	Minimum	Maximum	Average	Minimum	Maximum	Average
HT_0	3.577	3.592	3.585	3.583	3.600	3.594
HT_160	3.588	3.592	3.589	3.599	3.603	3.602
HT_480	3.587	3.590	3.589	3.600	3.604	3.602

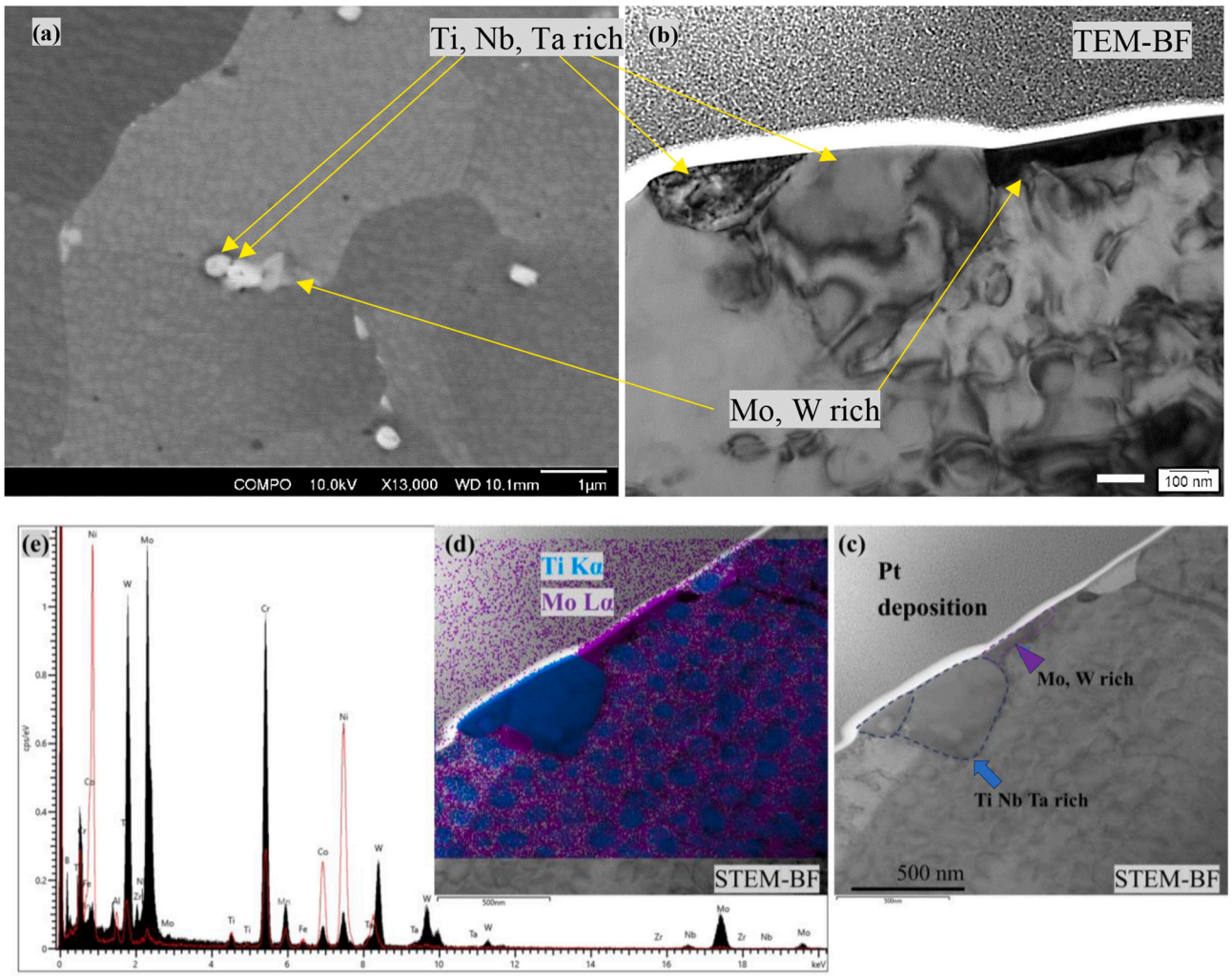

Fig. 9. (a) SEM micrograph of a plan view of two (Ti, Nb, Ta) rich particles and one (Mo, W) rich particle found after EDS mapping in HT_32. (b) TEM-BF micrograph after cross-sectional FIB thin foil preparation. (c) STEM-BF micrograph of the sample. (d) Identical to (c) but with superimposed EDS maps of Ti and Mo. (e) Representative EDS spectrum of Mo and W rich particle (boride) in solid and the comparative EDS spectrum of γ/γ′ in a line spectrum.

$[\bar{1}30]_{M5B3} \| [00\bar{1}]_{\gamma}$ and $(310)_{M5B3} \| (200)_{\gamma}$ as well as $(006)_{M5B3} \| (020)_{\gamma}$.

Using digitised electron intensity profiles from SAD patterns with the method and instrument applied in the current study in the range $1.5 < d < 2.0$ Å, enables to discuss lattice parameters with an accuracy of two decimal points in angstroms.

Fig. 15 shows an intragranular-type MC EDS map with HT_32. Fig. 16 shows the MC under a TEM-BF in a two-beam condition as well as a SAD at a $B = [001]_{MC}$. It is clear in Fig. 15 that MC is enriched with Ti. The Al map suggests γ′ are present 20–50 nm away from MC, as indicated by the dashed line delineating the MC morphology. A slight increase in Cr, Co and some Ni can be found as indicated by arrows in Fig. 15d-f close to the centre of the MC particle. The region was further observed under TEM-BF (Fig. 16a), which showed a dark region (see an arrow) and appeared to be nano scaled particles coinciding with the Cr, Co and Ni enrichment. It was also found that the SAD pattern in the region showed double diffraction that suggested the MC contains another phase coherent with the MC fcc based structure. Considering the enrichment of Ni, Cr and Co in the region, it is suggested that the region could contain fcc γ.

MCs appeared showing further evolutions after longer thermal exposure as shown in Fig. 17 taken from HT_160. Fig. 17a delineates multiple HAGBs, a twin boundary and an intergranular-type MC. It also shows an extremely fine grain sized <0.5 μm in width between the MC precipitate and the γ matrix: denoted as "Fine-G", divided by a low-angle GB (LAGB), which was confirmed with CBED patterns (Fig. 17b and c) from two regions A and B as indicated in Fig. 17d. By aligning the electron beam to $B = [011]_{MC}$, as shown in Fig. 18a, it was found the MC and Fine-G was separated across $(010)_{MC}$. EDS map results showed that fine γ′ particles present within Fine-G mentioned above, precipitated homogeneously, considering their spherical morphology (see Al map in Fig. 18e).

Quantitative chemical analyses of the metal elements, normalising to 100%, in borides can be found in Table 3 for M_5B_3 (the top row) of the two individual particles and for M_3B_2 (the bottom row) for HT_32 and HT_160 after averaging >15 individual particle analyses for each heat treatment. Fig. 19 shows a concentration relationship between Cr and Mo for individual M_3B_2 particles after 32 and 160 h, shown as circular and square data points, respectively. Cr and Mo have an inverse relationship, suggesting they are substituting for each other. It is also confirmed that Mo concentrations for a given Cr concentration in HT_160 are higher than those of HT_32.

4. Discussion

4.1. Considerations on M_5B_3 in new alloy

M_5B_3 type borides in Ni alloys have a tetragonal structure [30–32]. Space group of M_5B_3 have been discussed and many concluded to be I4/

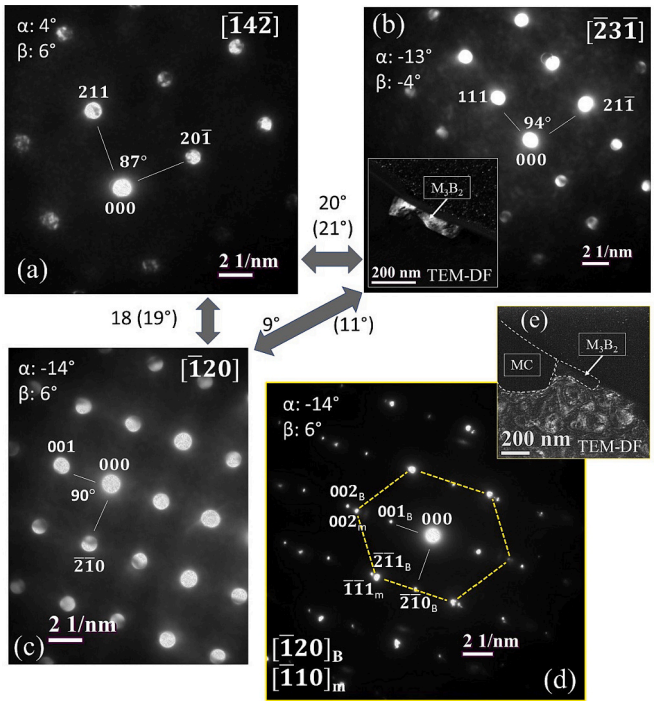

Fig. 10. (a)-(c) Three CBEDs from three different beam directions of the Cr Mo and W rich M_3B_2 found in Fig. 9. (b) has an inset with a TEM dark field (DF) micrograph of the M_3B_2. (d) composite SAD of M_3B_2 and a matrix (γ) present below the M_3B_2 at the same tilt angle to (c). (e) TEM-DF of the γ matrix.

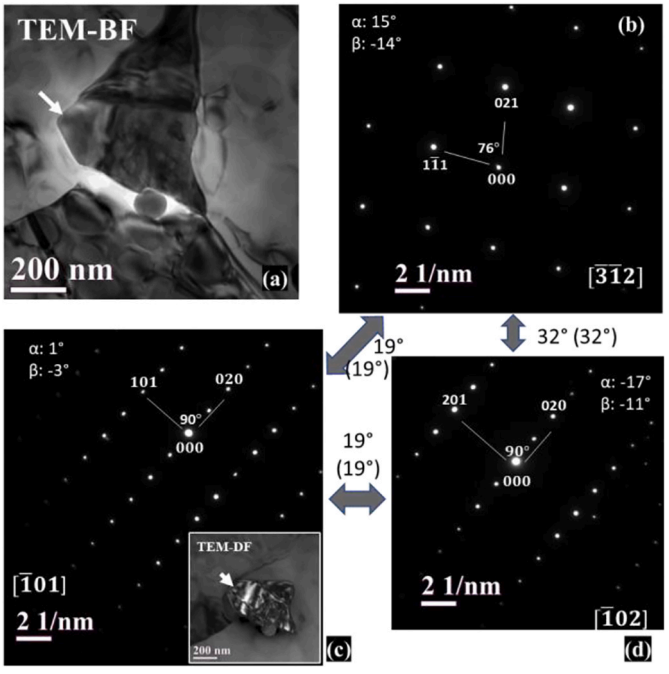

Fig. 11. (a) TEM-BF micrograph of a boride particle found in HT_32. (b)-(d) Three SADs from three different beam directions of the boride, identified as M_3B_2 type, including a DF micrograph (inset) in (c).

mcm [21,33,34], whose structure is schematically shown in Fig. 20. The structure should fulfil two conditions in diffractions, as follows [35,36]:

$$h+k+l=2n; \tag{1}$$

$$0kl\ h0l\ only\ when\ l=2n. \tag{2}$$

M_5B_3 in the current study revealed the presence of some reflections which should have been forbidden, for example (101) as seen in Fig. 12c and e, breaking the second condition of eq.2. However, the first condition (eq.1) was fulfilled in each SAD pattern. The finding agrees with other studies, including Ref. [21, 33] which suggested that it was due to dynamic electron reflections [21]. This can be interpreted that those forbidden spots can appear by multiple reflections (summations of multiple lattice vectors). In the current study, for example in Fig. 12c, the forbidden reflections of 101, 011, $\bar{1}0\bar{1}$, and $0\bar{1}\bar{1}$ shown as bright as other permitted similar $|\vec{g}|$ reflections, such as 110. It appears rather complicated to yield forbidden diffraction spots than a simple considerations based on multiple reflections.

The two M_5B_3 chemical analyses in Table 3 showed that the main metal elements were Cr, Mo and W with some trace elements, such as Ni, Nb and Ta. Dividing into groups of 1st, 2nd and 3rd row transition metal elements in the periodic table, suggesting nearly identical scattering factors for each other in each group in TEM, the composition can be calculated to be (Cr, Co, Ni): (Nb, Mo): (Ta, W) = 69:20:10. This can allow us to approximate the stoichiometry: $(Cr_{0.7}Mo_{0.2}W_{0.1})_5B_3$ with small substitutions of other alloying elements. Also significantly, the ratio can be rewritten as 14:4:2, considering the total metallic atoms in the unit cell of 20 in I4/mcm: M_5B_3. The fulfilling and breaking the two conditions can be due to a systematic atom-arrangement; potential ordering with metallic elements involved in the unit cell. This can be carried out mathematically by replacing two Mo atom pairs (in total 4 atoms) and one W pair (in total 2 atoms) in an I4/mcm: Cr_5B_3 structure (Fig. 20), so that keeping diffraction spots of $h+k+l\neq 2n$: absent, yet breaking (eq.2); this can be investigated by calculating each form factor: F for atom a for $(h\,k\,l)$ reflection in the unit cell, written as below;

$$F_{a(hkl)}=f_a[cos2\pi(hx_a+ky_a+lz_a)+isin2\pi(hx_a+ky_a+lz_a)] \tag{3}$$

where f_a is the scattering factor of atom a, occupying in $(x\,y\,z)$ in the unit cell, that generates one form factor for one atom in the unit cell for a diffraction plane.

Hu et al. [21] revealed atomic column images of M_5B_3 with partitioning of Mo and W, substituting Cr. The micrographs showed a clear indication of darkened atomic columns lining with Wyckoff 4c (four cyan atoms in Fig. 20) and concluded Wyckoff 4c was occupied by smaller metal atoms, e.g. Cr. This might be further understood via the distribution of boron atoms relative to the Wyckoff 4c position where a metal atom in this position is closely packed with six boron atoms within distances of 2.5 Å (see dashed lines in Fig. 20b), whereas, only four boron atoms for Wyckoff 16 l, making a tetrahedron with 4 borons on each corner with an average Cr-boron pair distance of 2.5 Å (see broken lines in Fig. 20b). Considering the smaller atomic radius of Cr (1.3 Å) than Mo and W (1.5 Å) [37], small atoms occupying Wyckoff 4c could be energetically favourable. Similar considerations can be applied to the Mo and W atom pairs which could favour avoiding these atoms in the metal-metal nearest neighbour (see a solid line in Fig. 20b). One of the suggested atomic configurations can be found in Fig. 21, including a three-dimensional view in Fig. 21b including visual support of the nearest neighbours explained above, together with simulated SAD patterns in Fig. 21c-f, following the beam directions from Fig. 12. The investigation above was based on retaining eq.1 to be fulfilled rather than based on the consideration of a potential ordering structure with the alloying elements to fulfil eq.2. A corresponding alternative Space group, specific to Fig. 21, has not been identified. Further studies are required. Presence and absence of the diffraction spots in the current study might be also affected by transformations to other boride species

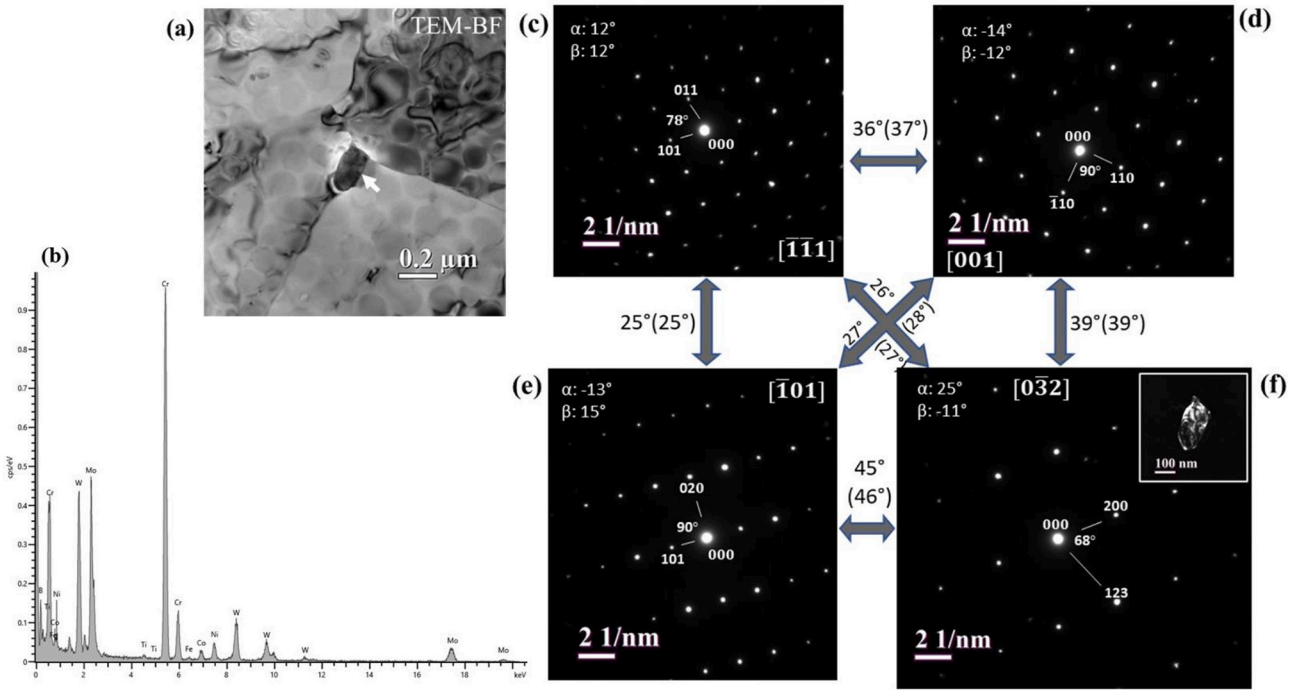

Fig. 12. (a) TEM-BF micrograph of a fine precipitate found in HT_32. (b) EDS spectrum of the fine precipitate. (c)-(f) SAD patterns of the precipitate at four different beam directions.

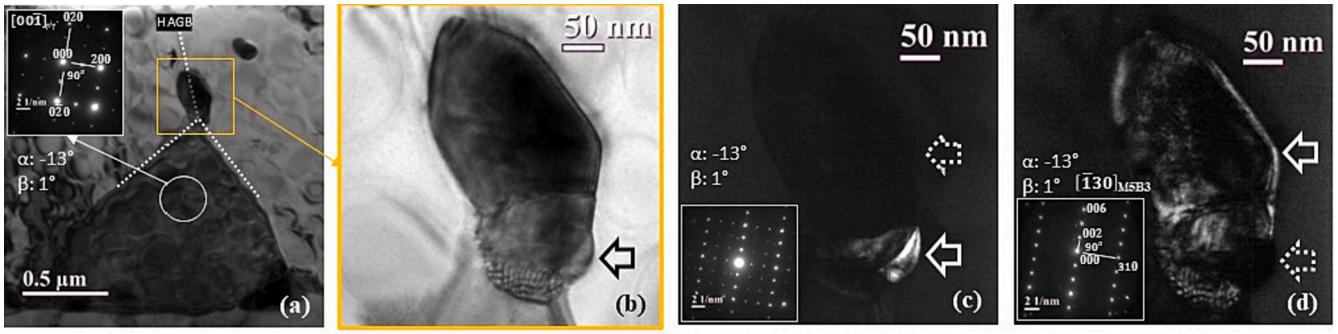

Fig. 13. (a) TEM-BF micrograph at a HAGB triple junction with an inset of a SAD pattern from the matrix, found in HT_32. (b) A magnified TEM-BF micrograph focusing on the particle. (c) TEM-DF micrograph of the fine precipitate, confirmed at the triple junction with its SAD pattern (inset). (d) TEM-DF micrograph of M_5B_3 precipitate surrounding the $M_{23}C_6$ precipitate, with the M_5B_3 SAD pattern (inset).

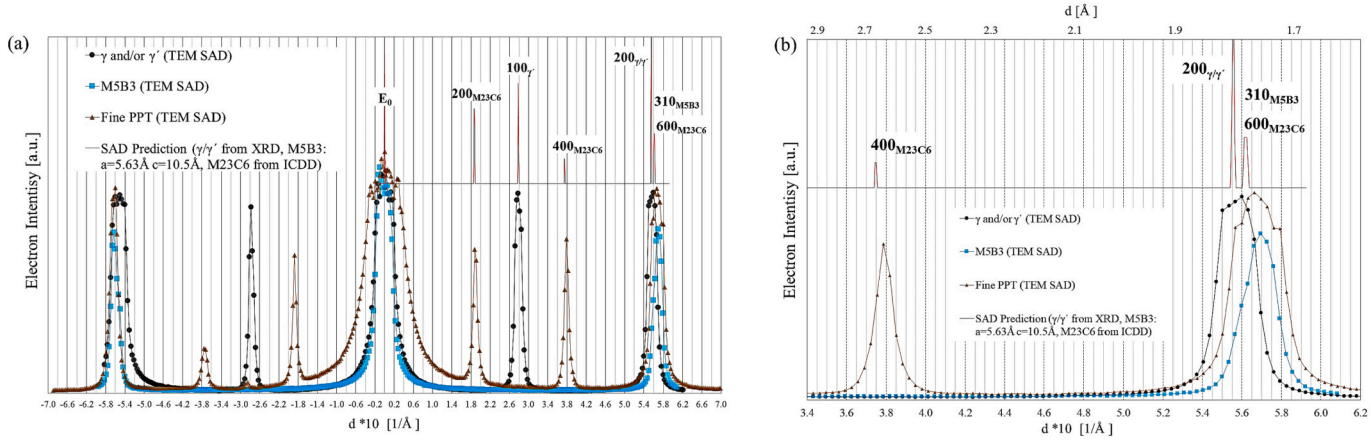

Fig. 14. (a) TEM SAD electron intensity profiles of M_5B_3, γ/γ´ and $M_{23}C_6$ along $(010)_{\gamma/\gamma'}$ and $(0\bar{1}0)_{\gamma/\gamma'}$, combined with simulated intensity profile along the same axis as the experimental results (top-right). (b) A magnified figure of (a) between 3.4 and 6.2 [1/Å*10] with an additional x-axis labelled in real space at the top.

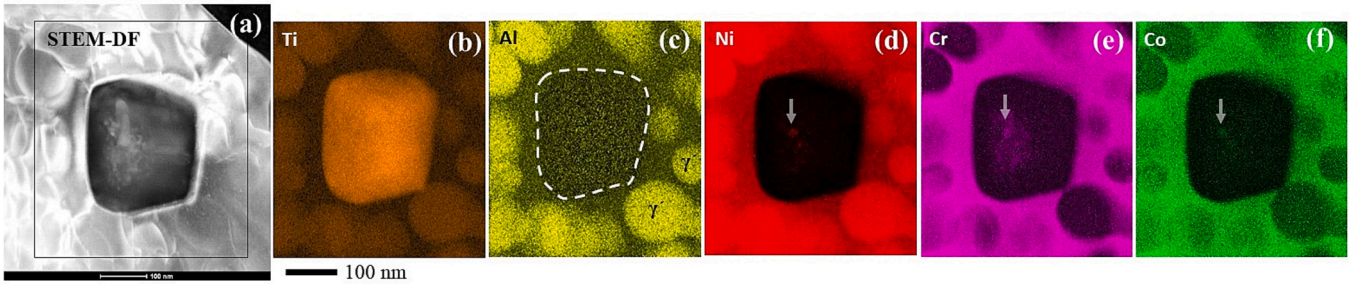

Fig. 15. (a) STEM-DF micrograph of MC particle using HT_32. (b)-(f) STEM-EDS maps of the MC with a small enrichment of Cr, Co and Ni (arrows).

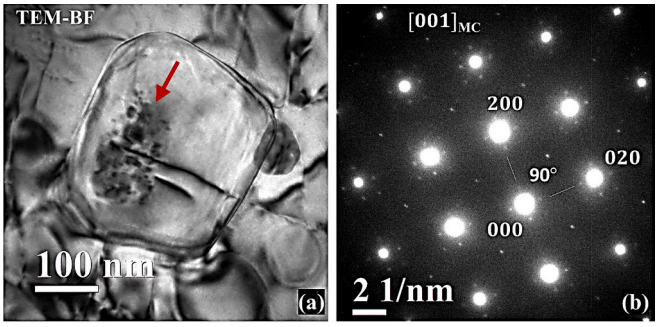

Fig. 16. (a) TEM-BF micrograph of the MC particle from Fig. 15. (b) SAD pattern from the MC and the Cr, Co and Ni enriched area, showing double diffraction with small satellite reflections around the main MC reflections.

which is further discussed in the following sections that could cause diffraction artefacts [38,39]. Regardless, the study above with the combination of TEM-SAD and EDS quantitative analyses and detailed calculations in understanding with a unit cell could provide insights to understand site occupancies, as a complementary analysis to high resolution electron microscopy and/or three-dimensional atom tomography.

4.2. Microstructural evolution

4.2.1. MC and borides evolution

In the as-quenched sample, the phases present were γ, γ′ and MC, which evolved by the precipitation of intergranular-type borides at the apparent expense of MC, as shown in Fig. 8a, suggesting MC decompositions started during the 32 h exposure. Regardless of the anti-correlation between the boride and MC fractions, the driving force for decomposition of the MC cannot be explained by the boride precipitation, because of the different chemistries of the two precipitates, which is also in line with the crystallographic coherencies of the boride with the γ-matrix regardless of the presence of the adjacent MC (Fig. 10), suggesting the borides nucleate at intergranular γ. After 32 h of the heat treatment, a crystallographic coherency between MC and nano-scaled γ particles was suggested by observing the double diffraction (Fig. 16). After further exposure to 160 h, the fine γ particles introduced earlier could coalesce and form a sub-micron grain, as noted "Fine-G" in Fig. 17–18, by forming an LAGB, containing fine and spherical γ′ particles inside. Throughout the thermal exposures, γ′ were rarely present adjacent to the MC, as shown by the EDS maps (Fig. 15). It is concluded that the MC decomposed to γ phase, with subsequent γ′ formation within the newly formed γ (Fig. 18).

At the early stage of the heat treatment, Cr rich $M_{23}C_6$ could nucleate. The precipitation could be also supported by the MC decomposition as suggested elsewhere [4]. However, in the current study, M_5B_3 was thermodynamically more stable, which prevented $M_{23}C_6$ growth, following the observation that fine $M_{23}C_6$ was surrounded by an coarser Cr-rich M_5B_3, as shown in Fig. 13. The observation above further reinforces discussion elsewhere [15] where systematic observations of alloys with different boron concentrations showed less or nil $M_{23}C_6$ in higher boron content alloys.

The presence of both M_5B_3 and M_3B_2 in a system have been reported elsewhere [21,40]. In the current system, M_5B_3 is concluded to be metastable by the size; finer than M_3B_2 and identified only after 32 h. M_3B_2, on the other hand, is concluded to be more thermodynamically stable because the precipitates are coarser and more numerous than those of M_5B_3. M_5B_3 has a coherent plane with the γ matrix: $(006)_{M5B3}\|(020)_\gamma$ (Fig. 13). M_3B_2 also has a coherent plane with the γ matrix: $(001)_{M3B2}\|(002)_\gamma$ (Fig. 10d), suggesting that both M_5B_3 and M_3B_2 can grow with their c axis parallel to $\{100\}_\gamma$. Hu et al. [21] observed stacking faults in an apparent boride particle along c: [001] axis in atom column imaging and concluded they were an intergrowth of the two borides M_3B_2 and M_5B_3, with similar a axis lattice parameters [21]. The intergrowth and/or phase transformations from M_5B_3 to M_3B_2 along c: [001] axis, parallel to $\{100\}_\gamma$, may occur in the current study.

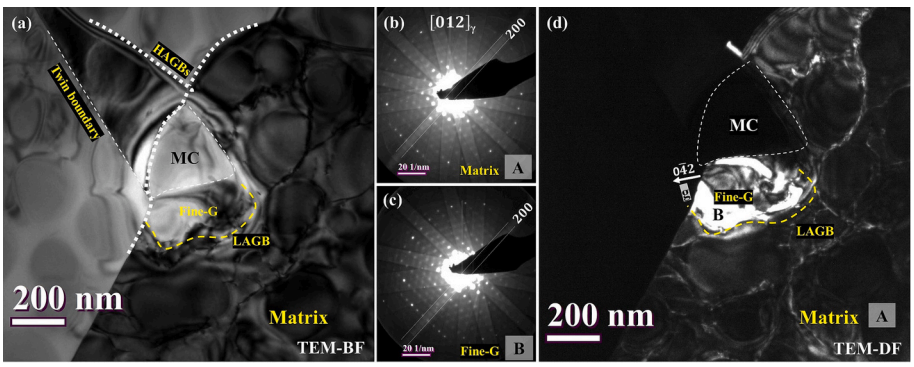

Fig. 17. (a) TEM-BF micrograph of HT_160, showing an MC precipitate is present close to a HAGB triple junction. (b)-(c) CBED Kikuchi patterns taken at the same tilt, but from the two different positions denoted A and B. (d) TEM dark field micrograph showing the regions A and B have different crystallographic orientations.

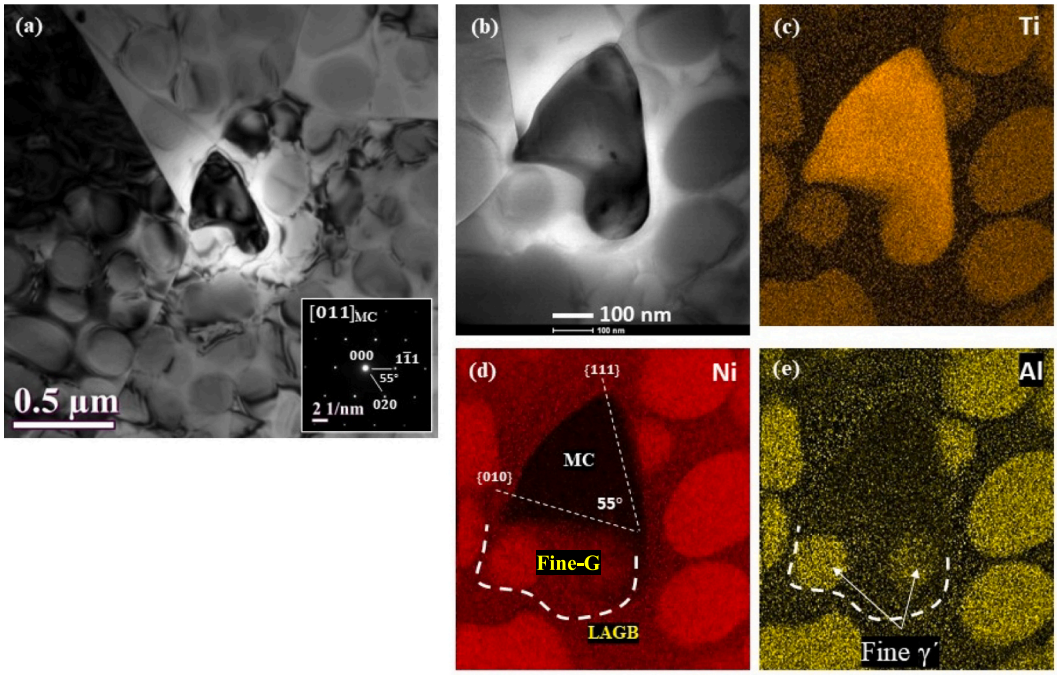

Fig. 18. (a) TEM-BF micrograph of the MC in Fig. 17 tilted to a zone axis [011]. (b) STEM-BF micrograph with the same TEM tilt angle as in (a). (c)-(e) EDS maps for Ti, Ni and Al, respectively.

Table 3
Summary of chemical analyses for metal elements in atomic percent (at.%) in the borides. The two M_5B_3 results were from the previously described TEM studies. The M_3B_2 results were averages and errors, calculated at 2σ after analysing >15 individual borides per thermal history.

Species / HT duration [at.%]		Al	Ti	Cr	Mn	Fe	Co	Ni	Zr	Nb	Mo	Ta	W
M_5B_3 (Fig. 12)	32 h	0.11	0.22	64.2	0.09	0.24	1.89	2.99	0.10	0.38	20.0	0.61	9.15
M_5B_3 (Fig. 13)		0.10	0.37	63.3	0.26	0.37	2.28	3.38	0.07	0.41	19.8	0.67	9.11
M_3B_2	32 h	Nil	1.2 ±0.2	38.7 ±2.3	Nil	0.4 ±0.2	3.2 ±0.5	5.1 ±0.5	Nil	3.3 ±0.7	34.4 ±1.6	1.3 ±0.5	12.0 ±0.5
	160 h	Nil	1.3 ±0.3	38.5 ±3.9	Nil	0.5 ±0.4	3.0 ±0.5	4.0 ±1.2	Nil	3.3 ±0.7	35.6 ±3.2	1.3 ±0.4	12.1 ±1.0

As shown in Fig. 19, the longer the thermal exposure the more the Mo concentration for a given Cr concentration in M_3B_2. It is worth noting that Mo can form Mo_3B_2 with the same Space group as V_3B_2 and with lattice parameters of a = 5.99 c = 3.14 Å (a/c = 0.524) [28], which is close to the current Mo rich M_3B_2 with deviations of <3% for each parameter, rather than V_3B_2, originally stated. In the current study, it can be safely concluded that metastable Cr-rich M_5B_3 are replaced by Mo-rich M_3B_2, although phase stabilities, particularly Mo_3B_2 in Ni based superalloys, have not been documented to the authors' knowledge. Further studies with theoretical predictions could provide insights, considering interactions with the matrix [41] as well as substitutions with other metals and interstitials within the precipitates [41,42].

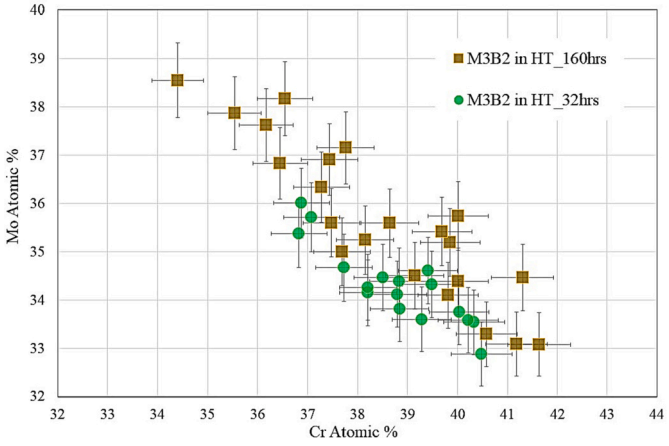

Fig. 19. Cr vs Mo concentration for M_3B_2 after 32 h in circles and 160 h in squares with the counting statistical error in 2σ (95% confidence).

Gupta et al. [19] found compositional gradients within an intergranular M_5B_3 type boride where Cr was enriched closer to the GB, which changed to W rich away from the GB. This was interpreted as a transformation to M_2B [19] and predicted that the formation of borides was a diffusion-controlled process [19]. The lattice diffusion coefficient of Mo at 900 °C: $0.9*10^{-16}$ m^2/s in fcc Ni [43] is appropriate to investigate our M_3B_2 coarsening kinetics. In the current study, the M_3B_2 coarsening kinetics can be estimated to correspond approximately to 10^{-23}-10^{-24} m^2/s, (e.g. Fig. 11 (0.3 µm in radius)), which resulted in a significantly slower M_3B_2 growth rate than the Mo diffusion rate in Ni fcc. Similar practice can be carried out with a longer exposure time with the SEM micrographs, e.g. Fig. 5 of 160 h. Considering the fast diffusion along grain boundaries, the differences is even more significant. This could be further discussed by different types of diffusions, such as ones in an ordered structure and Mo diffusion in Cr, as well as phase

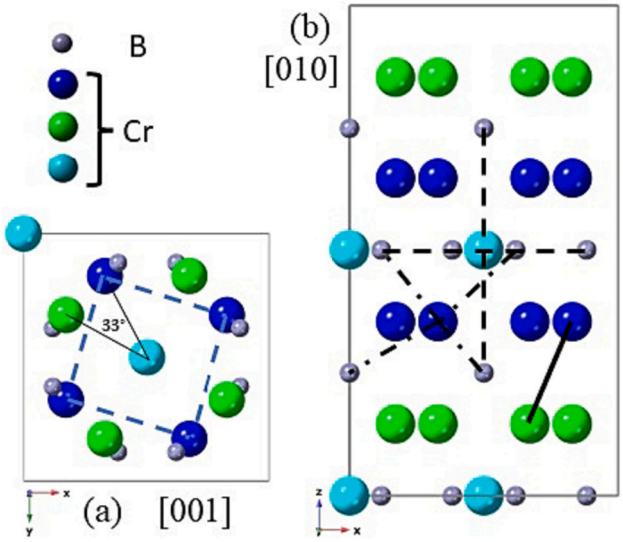

Fig. 20. I4/mcm Cr_5M_3 crystal structure visualised from two axes of [001] in (a) and [010] in (b). For the visual aid of the three-dimensional structure, Cr atoms are distinguished with cyan (Wyckoff 4c) and blue and green (Wyckoff 16 l). (For interpretation of the references to colour in this figure legend, the reader is referred to the web version of this article.)

transformations involved coarsening phenomena.

4.2.2. Driving force for MC decomposition

The effect of thermal exposure on borides and $M_{23}C_6$ formations in a Ni superalloy: IN792 at 900 °C were studied by Du et al. [31], where borides precipitated at an early stage but $M_{23}C_6$ started forming and coarsened at the expense of shrinking borides [31]. Fig. 22 shows predicted phase balances of γ′, MC and $M_{23}C_6$ in IN792 and New Alloy using Thermo-Calc, with the actual composition as mentioned earlier. IN792 showed close to 20% more γ′ fraction than New Alloy and importantly the major carbide was $M_{23}C_6$ at the 900 °C equilibrium. In each alloy, the onset of the MC decomposition in the ageing temperature regimes coincides with the precipitation of $M_{23}C_6$ and the discontinuous parabolic curve of the γ′ fraction (arrows in Fig. 22). To investigate further, using Thermo-Calc, the driving force of the MC decomposition in IN792 was investigated by changing the chemical compositions as shown in Table 4. AL792 decreased the Al concentration to the level of New Alloy by 0.33 wt%. In CB792, the carbon to boron ratio was changed to that of New Alloy, keeping the total fraction of carbon and boron identical to IN792. This was aimed at investigating the influence of borides, especially in relation to the metal elements Cr and Mo: the major partitioning elements in M_3B_2 and $M_{23}C_6$. Fig. 23a and b show the phase balance using the three alloys from Table 4, focusing on the onset temperatures of MC decomposition and comparing IN792 and AL792 and IN792 and CB792, respectively. There are clear differences in Fig. 23a in that MC became stable to a lower temperature: 949 °C in AL792 compared with 970 °C in IN792 as a result of reducing the Al concentration. The ratio of the interstitial elements affected the carbide/boride phase fractions but hardly changed the MC decomposition temperature (Fig. 23b). This suggests a minimal influence of Cr and Mo partitioning in M_3B_2 on the $M_{23}C_6$ precipitation driving force and hence on MC decomposition. Similar practices with other γ′ and MC partitioning elements, i.e. Ti, Nb, and Ta, were also examined. It was found that only Al, the main driving force to precipitate the Ni_3Al based γ′, showed such a prominent influence on the stability of MC. The prediction suggests MC decomposition can be affected by the γ′ precipitation driving force. In the current study: New Alloy at 900 °C, based on our microscopy-based observations, the driving force for decomposition of MC cannot be explained by the driving force to precipitate other carbide species, e.g. $M_{23}C_6$. Following the phase balance predictions using a high γ′ fraction superalloy close to

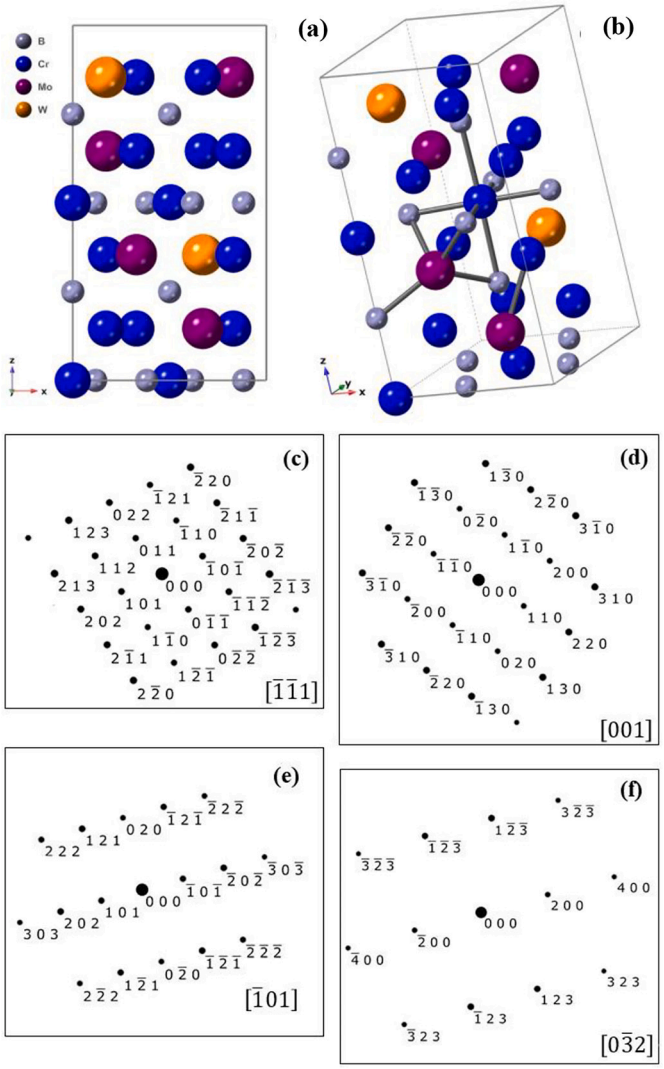

Fig. 21. (a) A possible $(Cr_{0.7}Mo_{0.2}W_{0.1})_5B_3$ atomic configurations viewed from [010] axis. (b) the same as (a) but titled to illustrate the structure three-dimensionally with the nearest neighbours mentioned in Fig. 20b. (c)-(f) corresponding simulated SAD patterns from four beam directions, following Fig. 12.

the temperatures of interest: 900 °C, it can be concluded that the γ′ precipitation driving force provides the primary driving force for the MC decomposition in the current study. As a summary, the flow chart below shows the sequence of the microstructural evolution found in the current system; the thick arrows indicate driving force to form phases; in some cases, with the aid of diffusion as indicated by thin arrows. Dashed lines indicate a reaction or phase which is extremely unstable and unconfirmed by SEM.

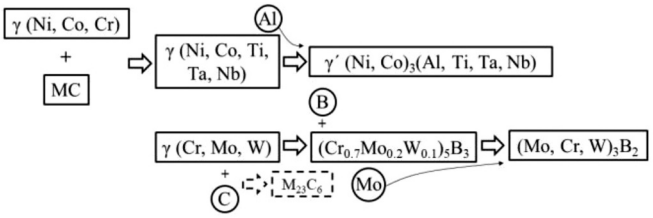

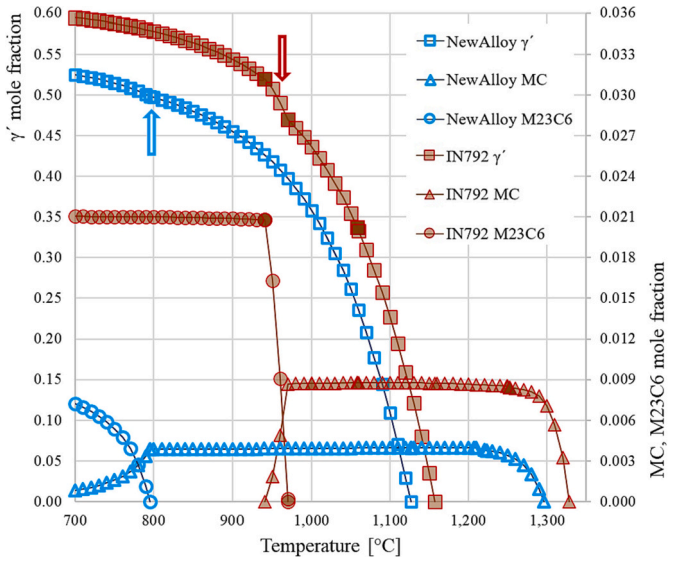

Fig. 22. Phase balance predictions using Thermo-Calc, comparing the two alloys: New Alloy and IN792. For clarity, only γ´, $M_{23}C_6$ and MC are shown.

5. Summary and conclusions

- After 480 h of iso-thermal treatment at 900 °C, the total area fraction of MC and borides was found to be approximately 0.6% while Thermo-Calc predicted 0.76%. Metastable Cr-rich M_5B_3 precipitated after 32 h but was not confirmed after 160 h. Instead, Mo-rich M_3B_2 became the major phase after γ and γ´, higher fraction than MC that reduced its fraction by approximately 50% compared to the as-quenched condition.
- The crystal structure of both M_5B_3 and M_3B_2 was tetragonal and the lattice parameters were determined as a = 5.63 c = 10.5 Å (c/a = 1.87) and a = 6.06 c = 3.23 Å (c/a = 0.533), respectively. The deviations from their prototypes: Cr_5B_3 and Mo_3B_2 were at a maximum of 3% for each parameter for the two species. Detailed SAD analyses including calibrations and digitised diffraction investigations, gave an accuracy of two decimal points in angstroms for a certain region of interplanar spacing.
- M_5B_3 was found to be a chemical composition: $(Cr_{0.7}Mo_{0.2}W_{0.1})_5B_3$. Using the chemistry, a potential ordering within a unit cell was discussed, although this is an open discussion with future work.
- M_5B_3 showed coherency with γ: $(006)_{M5B3}\|(020)_\gamma$. The c axis of M_3B_2 was parallel with the γ a axis. Provided that the metastable M_5B_3 transforms to, or intergrows [21] with M_3B_2, both borides can occur coherently along their c axes.
- $M_{23}C_6$ (a = 10.62 Å) was thermodynamically unfavoured over M_5B_3 and M_3B_2 which parabolically increased their fraction at 900 °C isothermal exposure. M_3B_2 coarsening had been considered to be a Mo diffusion-controlled process. However, the size of the M_3B_2 precipitates was significantly smaller than a data of the Mo diffusion rate in Ni. This could be attributed to simultaneous chemical evolutions within M_3B_2 such as Cr and Mo, as well as potential phase transformations from M_5B_3 to M_3B_2.
- Decomposition of MC can occur, with a sequential process leading to γ and the subsequent precipitation of γ´. The driving force of the MC decomposition was not attributed to other carbide formations. It was concluded to be primarily a γ´ precipitation driving force in order to increase its fraction to the equilibrium in the system at 900 °C.

Table 4
IN792 chemistry, taken from Ref. [31], and two modified model chemistries of AL792 and CB792 in weight percent (wt%).

ID /wt%	C	B	Al	Ti	Cr	Mn	Ni	Zr	Mo	Ta	W
IN792	0.089	0.014	3.43				59.7				
AL792			3.10	3.92	12.6	8.99	60.1	0.03	1.97	5.25	3.98
CB792	0.043	0.060	3.43				59.7				

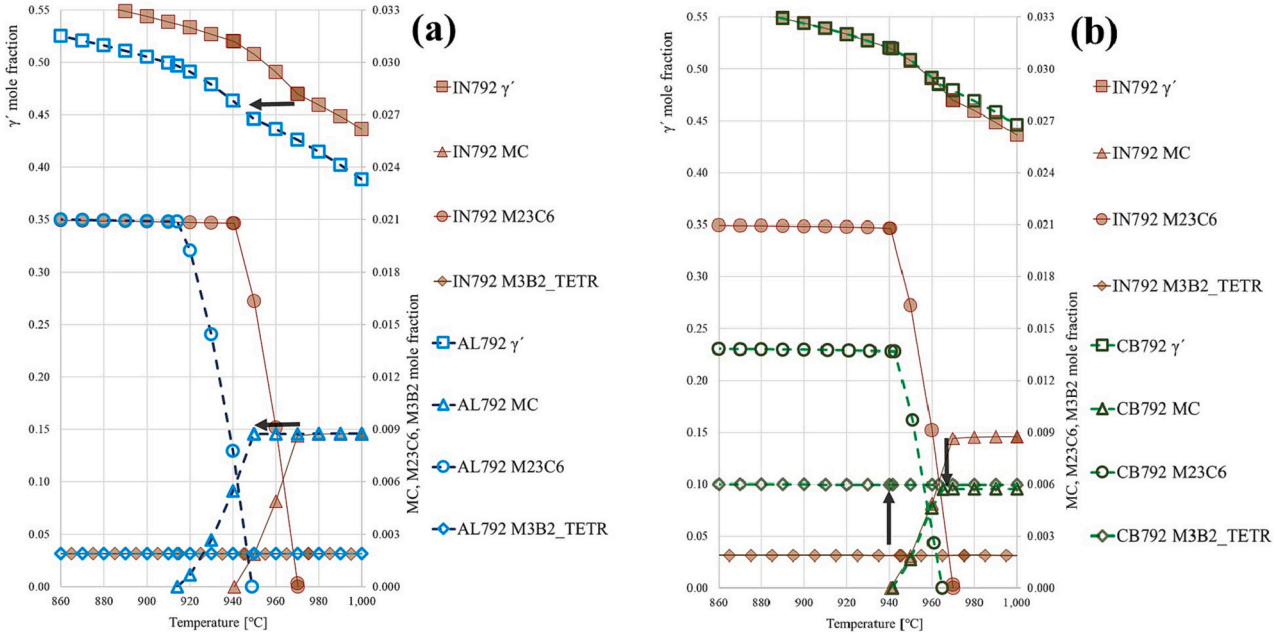

Fig. 23. Phase balance predictions using Thermo-Calc for γ´, $M_{23}C_6$, MC and M_3B_2 in the alloy systems introduced in Table 4. (a) comparison between IN792 and AL792. (b) comparison between IN792 and CB792.

CRediT authorship contribution statement

H.S. Kitaguchi: Conceptualization, Data curation, Investigation, Methodology, Writing – original draft, Writing – review & editing. **L. Small:** Data curation, Investigation. **I.P. Jones:** Supervision. **Y.L. Chiu:** Funding acquisition, Supervision. **M.C. Hardy:** Funding acquisition, Project administration. **P. Bowen:** Funding acquisition, Supervision.

Declaration of competing interest

The authors declare that there is no known competing financial interest or personal relationship that could have appeared to influence the work reported in the paper.

Data availability

Data will be made available on request.

Acknowledgement

The joint support of UK Engineering and Physical Science Research Council (EPSRC) and Rolls-Royce plc is greatly acknowledged. HSK and LS would like to thank Centre for Electron Microscopy (CEM) and Metallurgy&Materials Characterisation Facility at University of Birmingham for the support throughout the experimental investigations.

References

[1] C.T. Sims, W.C. Hagel, The Superalloys, Wiley-Interscience, 1972.
[2] R.C. Reed, The Superalloys: Fundamentals and Applications, Cambridge University Press, 2006.
[3] M.J. Donachie, Superalloys : A technical guide / Matthew J. Donachie, Steven J. Donachie, in: S.J. Donachie (Ed.), Materials Park, Ohio : ASM International, Materials Park, Ohio, 2002.
[4] H.E. Collins, Relative long-time stability of carbide and intermetallic phases in nickel-base superalloys, ASM (Am. Soc. Metals) Trans. 62 (1) (1969) 82–104.
[5] L.R. Liu, T. Jin, N.R. Zhao, X.F. Sun, H.R. Guan, Z.Q. Hu, Formation of carbides and their effects on stress rupture of a Ni-base single crystal superalloy, Mater. Sci. Eng. A (Struct. Mater. Prop. Microstruct. Process.) A361 (1–2) (2003) 191–197.
[6] G. Lvov, V.I. Levit, M.J. Kaufman, Mechanism of primary MC carbide decomposition in Ni-base superalloys, Metall. Mater. Trans. A Phys. Metall. Mater. Sci. 35 A(6) (2004) 1669–1679.
[7] X.Z. Qin, J.T. Guo, C. Yuan, J.S. Hou, L.Z. Zhou, H.Q. Ye, Long-term thermal exposure responses of the microstructure and properties of a cast Ni-base superalloy, Mater. Sci. Eng. A 543 (2012) 121–128.
[8] C. Baig Gyu, K. In Soo, K. Doo Hyun, J. Chang Yong, Temperature dependence of MC decomposition behavior in Ni-base superalloy GTD 111, Mater. Sci. Eng. A (Struct. Mater. Prop. Microstruct. Process.) 478 (1–2) (2008) 329–335.
[9] J. Wang, L. Zhou, X. Qin, L. Sheng, J. Hou, J. Guo, Primary MC decomposition and its effects on the rupture behaviors in hot-corrosion resistant Ni-based superalloy K444, Mater. Sci. Eng. A 553 (2012) 14–21.
[10] X.Z. Qin, J.T. Guo, C. Yuan, C.L. Chen, J.S. Hou, H.Q. Ye, Decomposition of primary MC carbide and its effects on the fracture behaviors of a cast Ni-base superalloy, Mater. Sci. Eng. A (Struct. Mater. Prop. Microstruct. Process.) 485 (1–2) (2008) 74–79.
[11] C.T. Liu, C.L. White, J.A. Horton, Effect of boron on grain-boundaries in Ni3Al†, Acta Metall. 33 (2) (1985) 213–229.
[12] L. Letellier, S. Chambreland, P. Duval, D. Blavette, Grain boundary segregation in nickel base superalloys Astroloy: an atom-probe study, IFES '92: 39th International Field Emission Symposium, 10-14 Aug 1992, Netherlands, 1993, pp. 305–310.
[13] D. Blavette, P. Duval, L. Letellier, M. Guttmann, Atomic-scale APFIM and TEM investigation of grain boundary microchemistry in Astroloy nickel base superalloys, Acta Mater. 44 (12) (1996) 4995–5005.
[14] T. Takasugi, N. Masahashi, O. Izumi, Electronic and structural studies of grain boundary strength and fracture in L12 ordered alloys. III. On the effect of stoichiometry, Acta Metall. 35 (2) (1987) 381–391.
[15] P. Kontis, H.A.M. Yusof, S. Pedrazzini, M. Danaie, K.L. Moore, P.A.J. Bagot, M. P. Moody, C.R.M. Grovenor, R.C. Reed, On the effect of boron on grain boundary character in a new polycrystalline superalloy, Acta Mater. 103 (2016) 688–699.
[16] P. Kontis, E. Alabort, D. Barba, D.M. Collins, A.J. Wilkinson, R.C. Reed, On the role of boron on improving ductility in a new polycrystalline superalloy, Acta Mater. 124 (2017) 489–500.
[17] P. Kontis, A. Kostka, D. Raabe, B. Gault, Influence of Composition and Precipitation Evolution on Damage at Grain Boundaries in a Crept Polycrystalline Ni-Based Superalloy, arXiv, 2019.
[18] L. Lilensten, A. Kostka, S. Lartigue-Korinek, S. Antonov, S. Tin, B. Gault, P. Kontis, On the Coarsening Mechanism and Deformation of Borides under Annealing and Creep in a Polycrystalline Superalloy, arXiv, 2020.
[19] R. Gupta, K.C.H. Kumar, M.J.N.V. Prasad, P. Pant, Compositionally graded nano-sized borides in a directionally solidified nickel-base superalloy, Scr. Mater. 201 (2021).
[20] X.B. Hu, Y.L. Zhu, X.L. Ma, Crystallographic account of nano-scaled intergrowth of M_2B-type borides in nickel-based superalloys, Acta Mater. 68 (2014) 70–81.
[21] X.B. Hu, Y.L. Zhu, N.C. Sheng, X.L. Ma, The Wyckoff positional order and polyhedral intergrowth in the M3B2- and M5B3-type boride precipitated in the Ni-based superalloys, Sci. Rep. 4 (1) (2014) 7367.
[22] M.C. Hardy, R.C. Reed, D. Crudden, Nickel-base superalloy, in: U.S. Patent (Ed.) United States Patent, USA, 2019.
[23] Q. Liu, An equation to determine the practical tilt angle of a double-tilt specimen holder and its application to transmission electron microscopy, Micron Microscop. Acta 20 (3–4) (1989) 261–264.
[24] H.S. Kitaguchi, I.P. Jones, C. Yulung, D. Rengen, M.C. Hardy, P. Bowen, Mesoscopic quantitative chemical analyses using STEM-EDX in current and next generation polycrystalline Ni-based superalloys, Ultramicroscopy 204 (2019) 55–72.
[25] Thermo-Calc Software TTNI8. https://thermocalc.com/, 2021.
[26] Crystal Maker Software SingleCrystal 4. https://crystalmaker.com/.
[27] D.M. Collins, L. Yan, E.A. Marquis, L.D. Connor, J.J. Ciardiello, A.D. Evans, H. J. Stone, Lattice misfit during ageing of a polycrystalline nickel-base superalloy, Acta Mater. 61 (20) (2013) 7791–7804.
[28] A. Wittmann, H. Nowotny, H. Boller, Ein Beitrag zum Dreistoff Titan-Molybdän-Bor, Monatshefte für Chemie und verwandte Teile anderer Wissenschaften 91 (4) (1960) 608–615.
[29] H.L. Yakel, Atom distributions in tau-carbide phases: Fe and Cr distributions in (Cr23-xFex)C6 with x=0, 074, 170, 413 and 736, Acta Crystallogr. Sect. B: Struct. Sci. 43 (3) (1987) 230–238.
[30] X.B. Hu, L.Z. Zhou, J.S. Hou, X.Z. Qin, X.L. Ma, Interfacial precipitation of the M<inf>5</inf>B<inf>3</inf>−type boride in Ni-based superalloys, Philos. Mag. Lett. 96 (7) (2016) 273–279.
[31] B. Du, L. Sheng, C. Cui, J. Yang, X. Sun, Precipitation and evolution of grain boundary boride in a nickel-based superalloy during thermal exposure, Mater. Charact. 128 (2017) 109–114.
[32] H.-R. Zhang, O.A. Ojo, Cr-rich nanosize precipitates in a standard heat-treated Inconel 738 superalloy, Philos. Mag. 90 (6) (2010) 765–782.
[33] H.R. Zhang, O.A. Ojo, M.C. Chaturvedi, Nanosize boride particles in heat-treated nickel base superalloys, Scr. Mater. 58 (3) (2008) 167–170.
[34] O.A. Ojo, H.R. Zhang, Analytical electron microscopy study of boron-rich grain boundary microconstituent in directionally solidified RENE 80 superalloy, Metall. Mater. Trans. A 39 (12) (2008) 2799–2803.
[35] D.E. Sands, D.H. Woods, W.J. Ramsey, The structures of Ba5Pb3, BaPb and BaPb3, Acta Crystallogr. 17 (8) (1964) 986–989.
[36] F. Bertaut, P. Blum, [X-ray] study of some chromium borides, Comptes Rendus Hebdomadaires des Seances de l'Academie des Sciences 236 (1953) 1055–1056.
[37] E. Clementi, D.L. Raimondi, Atomic screening constants from SCF functions, J. Chem. Phys. 38 (11) (2004) 2686–2689.
[38] C. Cayron, Diffraction artefacts from twins and stacking faults, and the mirage of hexagonal, polytypes or other superstructures, Scr. Mater. 194 (2021) 113629.
[39] K. Zhai, K. Zhao, Y. Zhang, J. Yue, P. Zhu, S. Li, C. Wang, C. Cui, D. Ping, Double diffraction or ω-Fe diffraction in body-centered cubic {112}⟨111⟩−type twinned martensite, Cryst. Growth Des. 23 (1) (2023) 539–547.
[40] N. Sheng, X. Hu, J. Liu, T. Jin, X. Sun, Z. Hu, M3B2 and M5B3 formation in diffusion-affected zone during transient liquid phase bonding single-crystal superalloys, Metall. Mater. Trans. A Phys. Metall. Mater. Sci. 46 (4) (2015) 1670–1677.
[41] R. Sahara, T. Matsunaga, H. Hongo, M. Tabuchi, Theoretical investigation of stabilizing mechanism by boron in body-centered cubic iron through (Fe,Cr)23(C, B)6 precipitates, Metall. Mater. Trans. A 47 (5) (2016) 2487–2497.
[42] M. Souissi, M.H.F. Sluiter, T. Matsunaga, M. Tabuchi, M.J. Mills, R. Sahara, Effect of mixed partial occupation of metal sites on the phase stability of γ-Cr23−xFexC6 (x=0–3) carbides, Sci. Rep. 8 (1) (2018) 7279.
[43] V.D. Divya, S.S.K. Balam, U. Ramamurty, A. Paul, Interdiffusion in the Ni–Mo system, Scr. Mater. 62 (8) (2010) 621–624.